Supporting Information for:

Matrix Isolation Spectroscopy and Nuclear Spin Conversion of Propyne Suspended in Solid Parahydrogen

A. I. Strom,[1] A. Gutiérrez-Quintanilla,[2,3a] M. Chevalier,[2] J. Ceponkus,[4] C. Crépin,[2] and D. T. Anderson*

[1]Department of Chemistry, University of Wyoming, Laramie, WY 82071-3838, USA

[2]Université Paris-Saclay, CNRS, Institut des Sciences Moléculaires d'Orsay, 91405, Orsay, France.

[3]Instituto Superior de Tecnologías y Ciencias Aplicadas (InSTEC), Universidad de La Habana, Ave. Salvador Allende No. 1110, Quinta de los Molinos, La Habana 10400, Cuba

[4]Institute of Chemical Physics, Vilnius University, Sauletekio ave. 9 III, LT-10222 Vilnius, Lithuania

[a)]Present address: Aix-Marseille Université, Laboratoire PIIM, Team ASTRO, Service 252, Saint Jérôme, Ave. Escadrille Normandie Niemen, 13013 Marseille, France.

*Author to whom correspondence should be addressed: danderso@uwyo.edu

Table of Contents

Table of Contents S1

1. Measuring Nuclear Spin Conversion Using a Parallel Band S2

2. Rovibrational Spectroscopy: Free versus Hindered Rotational Motion S4

3. Determining the *Para-to-Ortho* Ratio (POR) of Propyne Monomers in Solid pH_2 ..... S8

4. Supporting Figures S12

5. Supporting Tables S23

6. References S29

1. Measuring Nuclear Spin Conversion Using a Parallel Band

Difference spectra are calculated using the convention prescribed by Szczepanski *et al.*:[1]

$$\Delta A_t(\tilde{\nu}) \equiv A_t(\tilde{\nu}) - A_{t\to\infty}(\tilde{\nu}) = A_t - A_\infty$$

where $A_t(\tilde{\nu})$ is the decadic absorbance at time, t, and $t \to \infty$ is defined as the time at equilibrium. In order to quantify time-dependent intensity changes in overlapping, yet resolved peaks, of parallel (A_1-type) bands, calculated difference spectra are fit to an empirical lineshape model[2] composed of the sum of two normalized symmetric pseudo-Voigt profiles:

$$\Delta A_t(\tilde{\nu}) = \mathcal{A}_0 + \sum_{\lambda=1,2} [f_\lambda \mathcal{L}_\lambda(\tilde{\nu}, t) + (1 - f_\lambda)\mathcal{G}_\lambda(\tilde{\nu}, t)]$$

that is defined as a fractional sum of a normalized Gaussian profile, given by

$$\mathcal{G}_\lambda(\tilde{\nu}, t) = \frac{\mathcal{A}_\lambda(t)}{\gamma_{0,\lambda}} \sqrt{\frac{4\ln 2}{\pi}} \exp\left[-4\ln 2 \left(\frac{\tilde{\nu} - \tilde{\nu}_{0,\lambda}}{\gamma_{0,\lambda}}\right)^2\right]$$

and a normalized Lorentzian profile, given by

$$\mathcal{L}_\lambda(\tilde{\nu}, t) = \frac{2\mathcal{A}_\lambda(t)}{\pi\gamma_{0,\lambda}} \left[1 + 4\left(\frac{\tilde{\nu} - \tilde{\nu}_{0,\lambda}}{\gamma_{0,\lambda}}\right)^2\right]^{-1}$$

where $\mathcal{A}_0$ is a baseline correction, $\mathcal{A}_\lambda(t)$ is the time-dependent normalized area of peak λ (which is mathematically equivalent to the integrated absorbance), $\tilde{\nu}_{0,\lambda}$ is the wavenumber of the peak maximum, $\gamma_{0,\lambda}$ is the FWHM of the peak, and f_λ is the fraction of Lorentzian contributions to the total lineshape. Indeed, other lineshape models[3,4] are available, but the chosen model[2] efficiently extracts peak centers and areas for kinetics analyses with minimal systematic errors.[5] In passing, we note the previous utility of this model[2] in performing detailed fits to IR absorption spectra of *N*-methyl acetamide isolated in H_2 solids.[6]

For the case of two peaks in an overlapping spectrum, the indices λ = 1, 2 refer to the two components in the difference spectrum (*e.g.*, $\nu_2(A_1)$ of Fig. 2). The individual peak areas are conserved quantities and are directly extracted via this analysis in order to examine their time dependence. The time dependence of the two components in the difference spectra of ν_2 are well-fit to solutions of first-order kinetics equations of the form

$$para(E)\text{: } \mathcal{A}_{\lambda=1}(t) = \mathcal{A}_{\lambda=1}(\infty) + \left(\mathcal{A}_{\lambda=1}(0) - \mathcal{A}_{\lambda=1}(\infty)\right)e^{-t/\tau_{\lambda=1}}$$

$$ortho(A_1)\text{: } -\mathcal{A}_{\lambda=2}(t) = \mathcal{A}_{\lambda=2}(0) + \left(\mathcal{A}_{\lambda=2}(\infty) - \mathcal{A}_{\lambda=2}(0)\right)\left[1 - e^{-t/\tau_{\lambda=2}}\right]$$

The remaining parameters ($\tilde{\nu}_{0,\lambda}$, $\gamma_{0,\lambda}$, and f_λ) remain constant within the standard errors from the fits over the experimental timescale (δt) and are, thus, fixed to the average values for each experiment (see Table S3), reducing the number of fitted parameters needed for kinetics analyses. This simplifies the 9-parameter model above to a 3-parameter model (two peak areas $\mathcal{A}_{\lambda=1,2}(t)$ and a vertical offset $\mathcal{A}_0$ to correct for baseline jitter), significantly decreasing scatter in the fitted peak areas. With this, the effective lifetimes, τ_{eff}, of both components are determined to be statistically equivalent within the standard errors obtained from the fits (Table S4).

The original first-order kinetics equations employed by Szczepanski *et al.*,[1] given by

$$|A_t - A_\infty| = |A_0 - A_\infty|e^{-t/\tau}$$

are parametrized such that $A_t - A_\infty = 0$ at long times. As a caveat of the employed kinetics model, an artifact in $\mathcal{A}_\lambda(t)$ kinetic traces may arise (see Fig. 5(a)) in which the fitted curves cross through $A_t - A_\infty = 0$. This indicates that A_∞ was measured too early, before the system came into equilibrium. Fortunately, this does not affect the τ_λ values extracted from the fits due to the assumed first-order kinetics behavior, and this method to be used regardless of whether the true equilibrium was reached, so long as $\tau_{eff} < \delta t$ within reason (see Table S1).

2. Rovibrational Spectroscopy: Free versus Hindered Rotational Motion

The wavenumbers for rovibrational transitions of a free prolate symmetric rotor are given by[7,8]

$$\tilde{\nu}_{\text{gas}} = \tilde{\nu}_0 + F'(J,K) - F''(J,K),$$

where $\tilde{\nu}_0$ is the vibrational origin, $F(J,K)$ are the rotational term values, and single and double primes indicate upper and lower states, respectively. Reaching an upper vibrational level with A_1 or E type symmetry will then require parallel (A_1–A_1) or perpendicular (A_1–E) type band transitions, each with specific selection rules.[9] The rotational term values for the vibrational ground state ($v = 0$) and A_1–A_1 transitions to an upper level ($v > 0$) are given by

$$F(J,K) = B_v J(J+1) + (A_v - B_v)K^2 - D_J J^2(J+1)^2 - D_{JK} J(J+1)K^2 - D_K K^4$$

with selection rules $\Delta J = J' - J'' = 0, \pm 1$ and $\Delta K = K' - K'' = 0$, and $E \leftrightarrow E$ and $A_1 \leftrightarrow A_2$. Recall[7,8] that the first term corresponds to end-over-end J rotation perpendicular to the principal axis, the second term to single-axis K rotation about the principal axis, and the last three arise due to centrifugal distortion. The upper state term values of an A_1–E band are given by

$$F(J,K) = B_v J(J+1) + (A_v - B_v)K^2 - 2(A\zeta_i)_v lk - D_J J^2(J+1)^2 - D_{JK} J(J+1)K^2 - D_K K^4$$

with selection rules $\Delta J = 0, \pm 1$ and $\Delta K = \pm 1$, and $E \leftrightarrow E$ and $A_1 \leftrightarrow A_2$. In particular, note the additional first-order Coriolis coupling term,[8] in which ζ_i is the Coriolis coupling constant of mode i, the quantum number $l = v_i, v_i - 2, \ldots, -v_i$ is a projection of the vibrational angular momentum onto the principal rotational axis, and the projection $k = \pm K$; note that l-type doubling[10] responsible for splitting A_1 and A_2 levels (on the order of $\sim 2{B_v}^2/\tilde{\nu}_0$) is neglected as it is such a small effect. Accurate gas-phase spectroscopic constants of propyne and knowledge of the rovibrational selection rules for symmetric prolate tops are needed to calculate the transition wavenumbers of gaseous propyne, which are reported in Table 1 if possible. Typically, these transitions would be labelled using the conventional gas-phase notation ${}^{\Delta K}\Delta J_{v'}(J'', K'')$.

However, as discussed in the main body of the text, isolation of propyne within in a low-temperature matrix of solid pH$_2$ is thought to quench of the end-over-end rotational motion of the molecule, such that J is no longer well-defined and hence the energetic terms associated with end-over-end rotational motion are insignificant.[11] In this so-called hindered limit, we suggest a simpler, more concise transition notation, written as $\Delta K_{\upsilon'}(K'')$, for hindered (methyl) rotor molecules capable of undergoing single-axis[11] or internal[12,13] K rotational motion; this notation emphasizes that the "goodness" of J is lost, but neglects librational quantum numbers.

Consideration of only the rotational constants associated with one-dimensional K rotation yields (to a first approximation) the following expression for the rovibrational transition wavenumbers of a hindered prolate symmetric rotor suspended in a pH$_2$ matrix:

$$\tilde{\nu}_{\mathrm{pH_2}} \equiv \Delta K_{\upsilon'}(K'') = \tilde{\nu}_0 + F'(K) - F''(K)$$

Note that although this expression is mathematically equivalent to the sub-band origin:[7,8]

$$\tilde{\nu}_{gas}^{sub} = \tilde{\nu}_0 + F'(0,K) - F''(0,K)$$

which is a purely theoretical extrapolation to the J=0 limit, for the case to describe K rotation for a molecule suspended in solid pH$_2$ we use the J=K limit (and approximate $B_\upsilon = D_J = D_{JK} \equiv 0$).

Notwithstanding, neglecting libration and centrifugal distortion ($D_K' - D_K'' \approx 10^{-6}\ cm^{-1}$) and dropping subscripts for the vibrational dependence of the rotational constants, the rotational term values for an A_1 vibrational ground state and nondegenerate A_1 vibrational excited states are

$$F''(K) = A''K''^2 \ and \ \ F'(K) = A'K'^2$$

Hence, for A_1–A_1 transitions, the selection rule $\Delta K = 0$ holds, where substituting $K = K'' = K'$ and $\upsilon' = 1$ for a fundamental transition yields the Q-branch transitions:

$$Q_1(K) = \tilde{\nu}_0 + (A' - A'')K^2$$

For A_1–E fundamental transitions involving doubly degenerate E vibrational excited states ($\upsilon_i' = 1$ and $l = \pm 1$), the selection rule $\Delta K = \pm 1$ holds, so the rotational term values become

$$F'(K) = A'K'^2 \mp 2A'\zeta_i K'$$

For R-branch transitions ($\Delta K = +1,\ k \times l = +1$), substitution of $K' = K + 1$ (with $K = K''$) yields the following expression

$$\begin{aligned} R_1(K) &= \tilde{\nu}_0 + A'(K+1)^2 - 2A'\zeta_i(K+1) - A''K^2 \\ &= \tilde{\nu}_0 + (A' - A'')K^2 + 2A'(1-\zeta_i)K + A'(1-2\zeta_i) \end{aligned}$$

Similarly, for P-branch transitions ($\Delta K = -1,\ k \times l = -1$), substitution of $K' = K - 1$ yields

$$\begin{aligned} P_1(K) &= \tilde{\nu}_0 + A'(K-1)^2 + 2A'\zeta_i(K-1) - A''K^2 \\ &= \tilde{\nu}_0 + (A' - A'')K^2 - 2A'(1-\zeta_i)K + A'(1-2\zeta_i) \end{aligned}$$

Finally, insertion of K=0, 1, and 2 allows for the following simplified expressions to be obtained:

For parallel A_1–A_1 bands, three Q-branch lines are resultant:

$$Q_1(0) = \tilde{\nu}_0$$

$$Q_1(1) = \tilde{\nu}_0 + A' - A''$$

$$Q_1(2) = \tilde{\nu}_0 + 4(A' - A'')$$

For perpendicular A_1–E bands, two P- and three R-branch lines, five transitions are resultant:

$$P_1(2) = \tilde{\nu}_0 + A'(1 + 2\zeta_i) - 4A''$$

$$P_1(1) = \tilde{\nu}_0 - A''$$

$$R_1(0) = \tilde{\nu}_0 + A'(1 - 2\zeta_i)$$

$$R_1(1) = \tilde{\nu}_0 + 4A'(1 - \zeta_i) - A''$$

$$R_1(2) = \tilde{\nu}_0 + 3A'(3 - 2\zeta_i) - 4A''$$

All of which constitute an exhaustive list of the expected transitions of propyne isolated in solid pH$_2$ near lHe temperatures and observed via high-resolution matrix isolation FTIR spectroscopy.

One can remark that $R_1(2) - P_1(2) = 2[R_1(1) - P_1(1)]$ in this simplified model, in agreement with the gas phase values reported in Table 1.

Two *Q*-branch lines are resolved in the difference spectra of the A_1–A_1 bands observed: the pure vibrational transition out of the A_1, K''=0 ground state (equivalent to $\tilde{\nu}_0$) and the transition out of the *E*, K''=1 level of *ortho*- and *para*-propyne, respectively. Hence

$$Q_{v'}(1) - Q_{v'}(0) = A' - A''$$

From this, the general vibration-rotation interaction constant,[8,14] given by $A_v = A_0 - \sum_i v_i \alpha_i^A$, can be rearranged for our purposes (neglecting anharmonicity) as

$$A' - A'' = A_v - A_0 = -\sum_i v_i \alpha_i^A$$

Several parallel bands were resolved via the difference spectra fitting procedure detailed above, for which measured and gas-phase vibration-rotation constants are contrasted in Table S3.

Further, generating linear combinations of the various transition wavenumber equations in $K'' = K$ allows one to derive equations for the rovibrational constants of a hindered methyl rotor (*e.g.*, propyne isolated in a solid *p*H_2 matrix). First of all, using the equations for $P_1(1)$, $R_1(0)$, and $R_1(1)$ above, the following system of equations have been derived[11] which prove useful for analysis of three-line perpendicular band systems if a value of the Coriolis constant is assumed, or fixed to the gas-phase value:

$$\frac{R_1(1) - P_1(1)}{4} = A'(1 - \zeta_i)$$

$$\frac{R_1(1) - 2R_1(0) + P_1(1)}{2} = A' - A''$$

$$\frac{P_1(1) + 2R_1(0) - R_1(1)}{2} = \tilde{\nu}_0 - A'$$

This is in fact equivalent to fitting the transition wavenumbers for these three rovibrational transitions to the following quadratic equation:

$$E(m) = \tilde{\nu}_0 + (A' - A'')m^2 + 2A'(1 - \zeta_i)m + A'(1 - 2\zeta_i)$$

Where $m = K''$ is substituted for *R*-branch lines ($E(m) = R_1(K)$) and $m = -K''$ is substituted for *P*-branch lines $E(-m) = P_1(K)$) in the fitting algorithm. This procedure was verified by reproducing the values reported in Ref. 11. This analysis can be extended to $P_1(2)$ and $R_1(2)$ transitions as well. Also, an effective centrifugal distortion constant may "correct" the ground state rotational term value:

$$F''(K) = A''K''^2 - D''_{K,\text{eff}}K''^4$$

such that the following equation is fit as described above:

$$E(m) = \tilde{\nu}_0 + (A' - A'')m^2 + 2A'(1 - \zeta_i)m + A'(1 - 2\zeta_i) + D''_{K,\text{eff}}m^4$$

Please see the main text for more discussions on fitting perpendicular-type band spectra.

3. Determining the *Para-to-Ortho* Ratio (POR) of Propyne Monomers in Solid *p*H_2

The rotational term values for the ground vibrational state ($v = 0$) of a prolate symmetric top[7,8] including centrifugal distortion corrections in the free-rotor limit are given by

$$F(J,K) = B_0J(J+1) + (A_0 - B_0)K^2 - D_JJ^2(J+1)^2 - D_{JK}J(J+1)K^2 - D_KK^4$$

With this, the rotational energy level diagram shown in Fig. S7 is calculated using the conventional ground state rotational constants for propyne including centrifugal distortion.[15] For completeness, these ground state energy levels can be used to calculate the transition wavenumbers, $\tilde{\nu}_{\text{gas}}$ (introduced in the previous section), for various rovibrational transitions such as $\nu_2(A_1)$,[16,17] $\nu_6(E)$,[18] and $\nu_7(E)$,[19] which are shown in Fig. S8, illustrating the various selection rules of a prolate symmetric top.[7-9] The inability to determine both upper and lower state constants adequately prevents calculation of the corresponding transition energies for propyne in solid *p*H_2 (see manuscript).

Both the *ortho* and *para* nuclear spin isomers are coupled to specific nuclear spin (*I*) and rotational (*J,K*) quantum numbers and their populations are weighted by the corresponding degeneracies (g_I and g_{KJ}), summarized in Table S0 below.[7,8] The *para-to-ortho* ratio (POR) is generally defined[20] as the ratio of the rotational partition functions of the *para* and *ortho* nuclear spin isomers:

$$POR = \frac{Q^{rot}_{para}(T)}{Q^{rot}_{ortho}(T)} = \frac{2\sum_{J,K\neq 3n} g_{KJ} e^{-\beta F_{para}(J,K)}}{4\sum_{J,K=3n} g_{KJ} e^{-\beta F_{ortho}(J,K)}}, \qquad J \geq K, \qquad n = 0,1,2, \ldots$$

where $\beta = 1/k_B T$ is a temperature dependent factor, $k_B \approx 0.695\, cm^{-1}\, K^{-1}$ is Boltzmann's constant, $F(J,K)$ are the corresponding rotational term values in the $v = 0$ state,[15] and the weights g_I and g_{KJ} are listed in Table S0 below; note that excited vibrational state populations are negligible at sufficiently low temperatures ($Q^{vib} \approx 1$). The theoretical POR curve of propyne is plotted in Fig. S7 using the calculated gas-phase ground state energy level diagram.

Table S0. Nuclear spin and rotational weights for a prolate symmetric top with C_{3v} symmetry containing I=½ nuclei in the free (gas) and hindered (pH$_2$) rotor limit.

Nuclear Spin Isomer	Rot. Symm.	I	g_I	gas ($J \geq K$)		pH$_2$ ($J = undefined$)	
				K	g_{KJ}	K	g_K
para	E	$^1/_2$	2	$\neq 3n$	$2(2J+1)$	$\neq 3n$	2
ortho	A_1	$^3/_2$	4	0 $3n > 0$	$2J+1$ $2(2J+1)$	$3n \geq 0$	1

In order to measure the POR of propyne isolated in solid pH$_2$, we rely upon previous matrix isolation studies on the *ortho*-to-*para* NSC of H$_2$O isolated in rare-gas matrices.[21-23] The total intensity (integrated absorbance) of a transition between an initial state i to a final state f is

$$I_{if} = \int A_{if}(\tilde{\nu}) d\tilde{\nu} = F_{if} n_i$$

where F_{if} is the temperature-independent linestrength for the transition $i \rightarrow f$ and the average population of the initial state is simply expressed as a Boltzmann distribution:

$$n_i = \frac{g_i e^{-\beta E_i}}{Q(T)}$$

It follows that the population ratio is equivalent to the Boltzmann factor at thermal equilibrium

$$\frac{n_i}{n_{i'}} = \frac{I_{if}/F_{if}}{I_{i'f'}/F_{i'f'}} = \frac{g_i}{g_{i'}} e^{-\beta(E_i - E_{i'})}$$

where the total population $\sum_i n_i = constant$. Specifically, for *para*- ($i = K'' = 1$) and *ortho*-propyne ($i' = K'' = 0$) isolated in solid pH$_2$, the expressions above are valid if the first two *K*-rotor states are the only ones with significant population between 1.7 – 4.0 K, and the total number of *ortho*- and *para*-propyne molecules remains constant. Thus, at thermal equilibrium

$$POR_{eq} = \frac{n_{K''=1}}{n_{K''=0}} = \frac{n_{para}}{n_{ortho}} = \frac{g_{para}}{g_{ortho}} \exp[-\beta(E_{K''=1} - E_{K''=0})]$$

If *J* is not well defined, then the 3D rotational wavefunctions[7] (see text for details) should collapse to those of a 1D particle-on-a-ring ($\propto e^{\pm iK\varphi}$) with rotational eigenenergies given by $A_0 K^2$ in the $v = 0$ state. In this approximation, the total weights ($g = g_I g_{KJ}$) for the two states cancel fortuitously, that is $g_{para} = 2 \times 2$ (assuming that the rotational degeneracy is simply *two* for 1D single-axis rotation with *K*″=1) and $g_{ortho} = 4 \times 1$ (see Table S0). The energy difference between the first two *K*-rotational levels of propyne $E_1 - E_0 \approx A''_{\text{eff}}$ is related to an effective (perturbed) ground state A_0 rotational constant of propyne in solid pH$_2$. The energy diagram of propyne undergoing pure *K*-rotation with $F(K) = A_0 K^2$ is given in Fig. S9.

This energy difference is best determined for relatively well-isolated rovibrational band transitions. Case in point, the ν_6 $R_1(0)$ ($K'' = 0 \rightarrow K' = 1$) and $R_1(1)$ ($K'' = 1 \rightarrow K' = 2$)

transitions of *ortho*- and *para*-propyne, respectively. Assuming *all ortho*- and *para*-propyne molecules occupy the two lowest K'' rotational levels, and the total population

$$n_{K''=0} + n_{K''=1} = \frac{I_{01}}{F_{01}} + \frac{I_{12}}{F_{12}} = constant \approx 1$$

it follows[22] that

$$I_{12} = -\frac{F_{12}}{F_{01}} \times I_{01} + F_{12} \Leftrightarrow y(x) = sx + y_0$$

That is, the integrated intensities of the ν_6 $R_1(0)$ and $R_1(1)$ transitions are linearly correlated,[21] as shown in Fig. S10, where the slope of the correlation-plot ($s = -F_{12}/F_{01}$) is associated with the relative line strength of the transitions in consideration. The ν_6 $R_1(1)$ vs. $R_1(0)$ data was used preferentially because of improved spectral isolation and less overlap with non-rotating peaks in the integration regions relative to the $P_1(1)$ vs. $R_1(0)$ data (Fig. S4); least-squares fitted parameters to all possible ν_6 intensity-intensity correlation plots are provided in Table S5. The sum of the ν_6 $P_1(2)$ and $R_1(2)$ integrated intensities comprises ≤ 5% of the total ν_6 band area ($n_{K''=2} \approx 0$), indicating a relatively small thermalized propyne population, so this assumption holds quite well.

As shown in Fig. 6 of the main text, the time-dependence of the propyne POR due to *ortho-to-para* NSC in solid *p*H_2 is found to decay exponentially as

$$POR_t = \frac{n_{para}(t)}{n_{ortho}(t)} = \frac{I_{12}(t)}{I_{01}(t)}\left|\frac{F_{12}}{F_{01}}\right|^{-1} = POR_\infty + (POR_t - POR_\infty)e^{-k_{POR}t}$$

Where thermal equilibrium is achieved at the asymptote $t \to \infty$. Therefore, the effective ground state rotational constant of propyne isolated in solid *p*H_2 can be calculated at thermal equilibrium via equating the Boltzmann and asymptotic POR expressions ($POR_{eq} = POR_\infty$) above, yielding

$$POR_\infty = \frac{I_{12}(\infty)}{I_{01}(\infty)}\left|\frac{F_{12}}{F_{01}}\right|^{-1} = \frac{2 \times 2}{4 \times 1}\exp[-\beta(E_{K=1} - E_{K=0})] = \exp\left[-\frac{A''_{\text{eff}}}{k_B T}\right]$$

$$\Rightarrow A''_{\text{eff}} = -k_B T \ln(POR_\infty) = 2.22(55)\ cm^{-1}$$

Which is determined using the fitted parameters F_{12}/F_{01} and POR_∞ from least squares fits to intensity-intensity correlation plots and intensity ratios for the ν_6 $R_1(1)/R_1(0)$ data, respectively, as the weighted average over six kinetic runs (see Tables S4 and S6).

The observed first-order *para-to-ortho* NSC kinetics of propyne isolated in solid *p*H_2

$$para - \mathrm{H_3CC_2H} \xrightarrow{k_{eff}} ortho - \mathrm{H_3CC_2H}$$

was initially quantified using an effective time constant $\tau_{eff} = 1/k_{eff}$ (Table S4). Given that the energy gap between the first two K'' levels is so small, higher rotational levels should be sufficiently populated such that NSC becomes a reversible first-order process, given by

$$ortho - \mathrm{H_3CC_2H} \underset{k_{p\to o}}{\overset{k_{o\to p}}{\rightleftharpoons}} para - \mathrm{H_3CC_2H}$$

Because the effective rate constant is defined as the sum of the forward (*ortho→para*) and reverse (*para→ortho*) rate constants

$$k_{eff} = k_{o\to p} + k_{p\to o}$$

The concept of microscopic reversibility requires that the equilibrium constant[23] obeys

$$K_{eq} = \frac{[para - \mathrm{H_3CC_2H}]}{[ortho - \mathrm{H_3CC_2H}]} = \frac{k_{o\to p}}{k_{p\to o}} = POR_\infty$$

in which the denominator is defined as the state incurring increasing population. Thus, the forward and reverse NSC rate constants are expressed as,

$$k_{p\to o} = \frac{k_{eff}}{1 + POR_\infty},$$

$$k_{o\to p} = \frac{k_{eff} POR_\infty}{1 + POR_\infty}$$

which have been calculated using exclusively the ν_6 data of Table S4 and tabulated in Table S6.

4. Supporting Figures

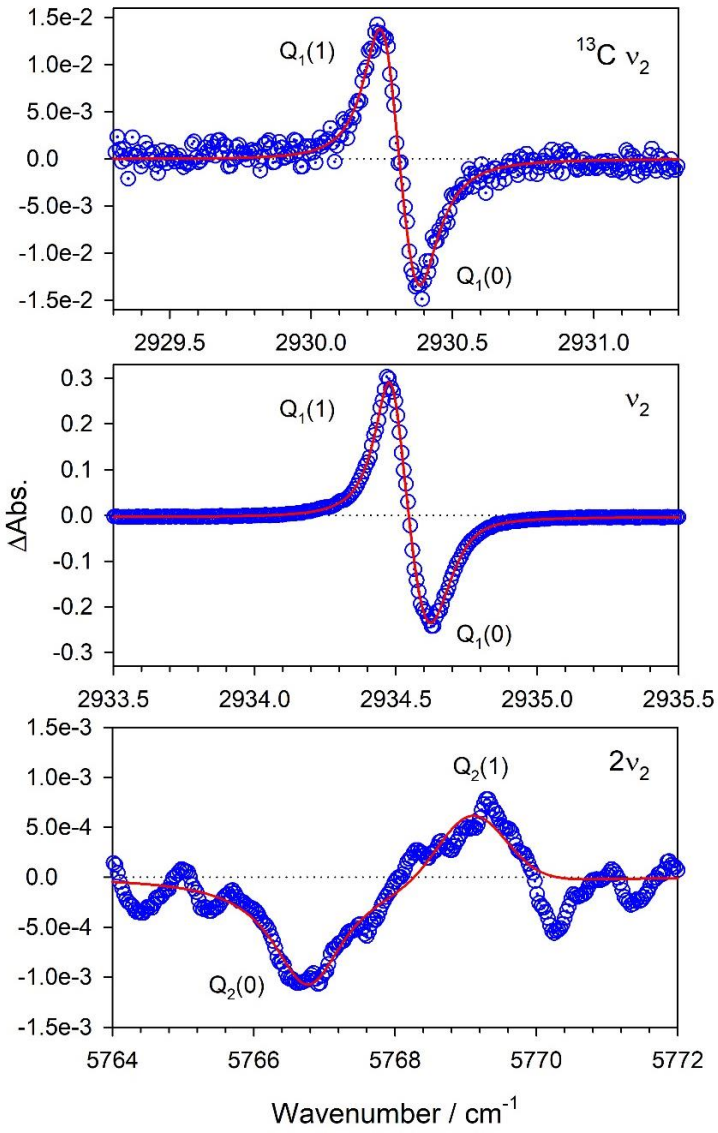

Figure S1. Comparison of difference spectra for the ν_2 fundamental of $^{13}CH_3{}^{12}C_2H$ (top) and the ν_2 (center) and $2\nu_2$ (bottom) modes of $^{12}CH_3{}^{12}C_2H$ isolated in solid pH$_2$. Measured (A_0–A_∞) difference spectra (blue circles) are fit to the sum of two pseudo-Voigt lineshapes (red line). The center trace shows changes over ~5 h [Expt. 2; 74(10) ppm, d=2.17(2) mm, T=1.72(1) K], while the top and bottom traces are from a concentrated sample after ~6.5 h [Expt. 5; 289(16) ppm, d=2.51(3) mm, T=1.72(2) K]. Top: ν_2 of $^{13}CH_3{}^{12}C_2H$ exhibits a splitting nearly identical to ν_2 of the normal isotopologue. Center: shown for comparison (see Figs. 2 & 4). Bottom: The $2\nu_2$ splitting is large and negative relative to ν_2; fitting this spectrum required extensive signal processing (as shown in Fig. S3). Table S3 contains fitted parameters and details of the fits.

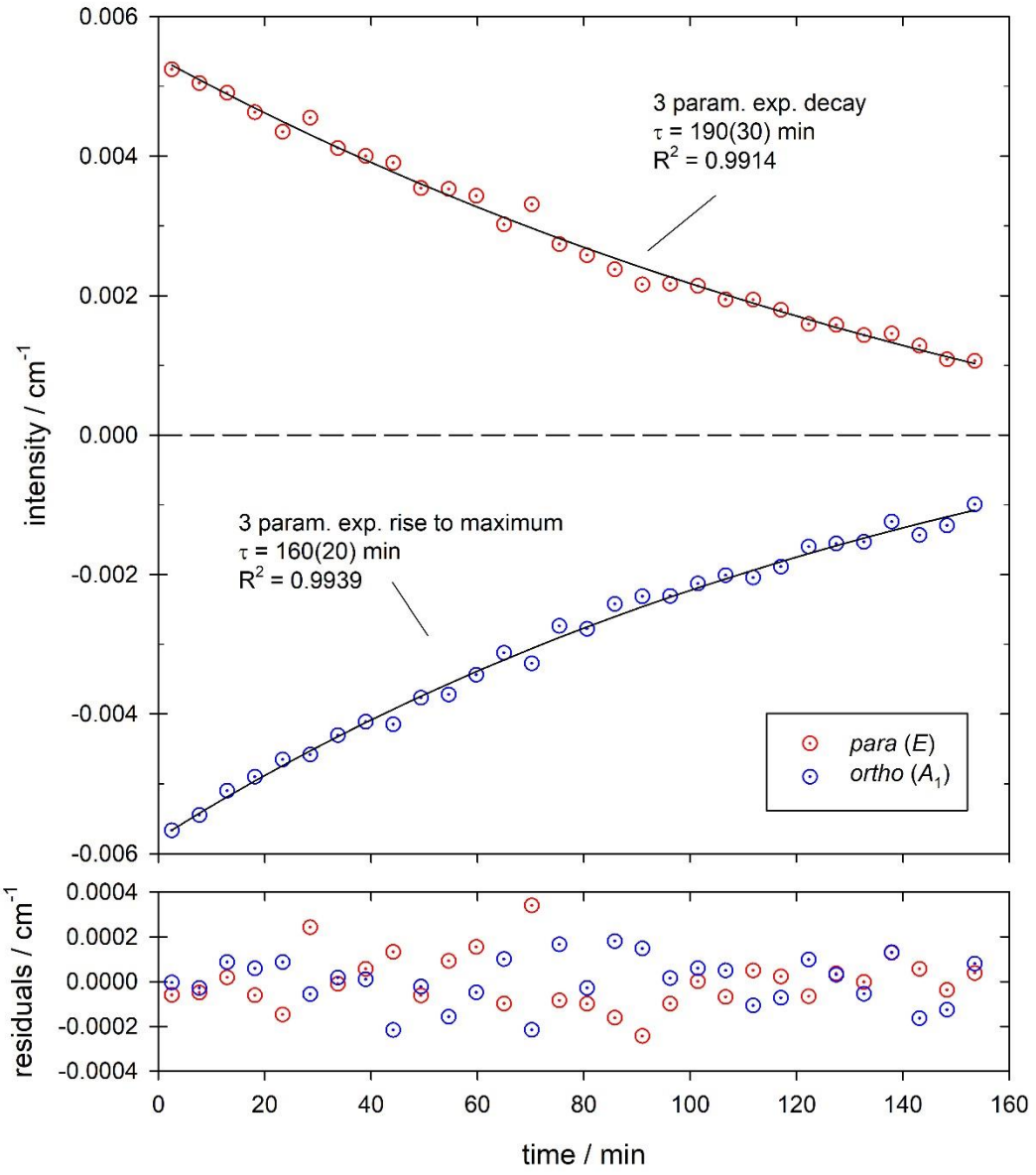

Figure S2. Kinetic traces for the *ortho-to-para* NSC of the mono-substituted ^{13}C isotopologue of propyne ($^{13}CH_3{}^{12}C_2H$) isolated in solid pH_2 present in natural isotopic abundance (~1.1%) after deposition. The first data point (A_0–A_∞) corresponds to the ν_2 difference spectrum in Fig. S1 (top). The NSC kinetic traces are obtained by fitting the ν_2 difference peak areas (extracted from 3-parameter pseudo-Voigt fits) to a first-order kinetics model. These pseudo-Voigt fits employ fixed parameters obtained from an initial 9-parameter fit to the spectrum in Fig. S1 (provided in Table S3). The weighted average of the effective time constants provided in the figure is $\tau_{eff,13}$ = 170(20) min, which is 1.7(2) times greater than the global weighted average effective time constant of $^{12}CH_3{}^{12}C_2H$ ($\tau_{eff,12}$ = 287(7) min; Table S4).

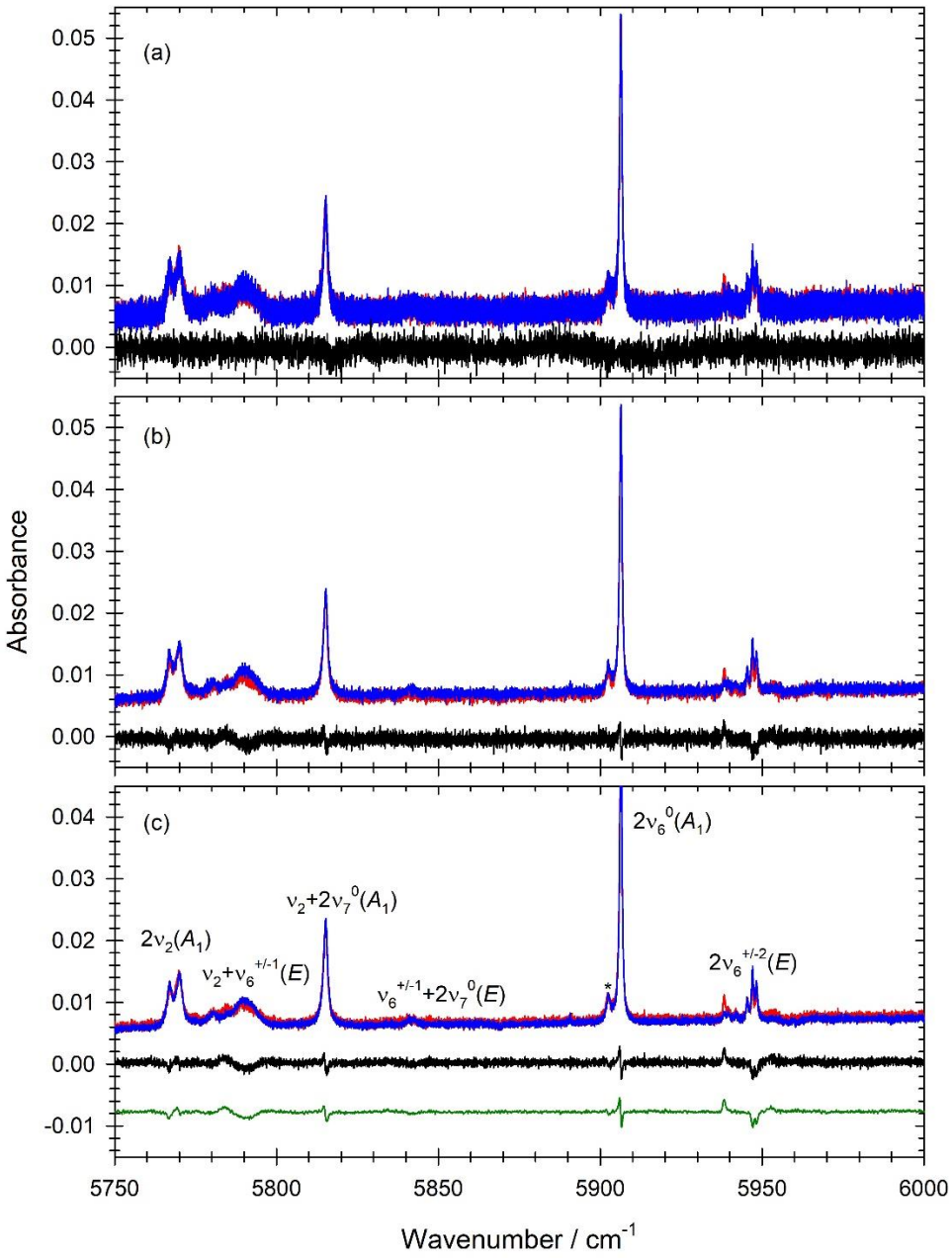

Figure S3. The methylic C–H stretch overtone region of propyne in solid *p*H_2 illustrating effects of signal processing. The red, blue, and black traces correspond to as-deposited (t=0), equilibrium post ~6.5 h ($t\rightarrow\infty$), and difference spectra (A_0–A_∞) from Expt. 5, respectively. (a) High-resolution (0.02 cm^{-1}) spectra, exhibiting initially poor S/N. (b) The same spectra from (a) with degraded resolution (0.1 cm^{-1}), exhibiting improved S/N. (c) Spectra from (b) now with averaging and vibrational assignments (see Ref. 24): the red and blue traces are now the average of the first two and the last four spectra collected during the NSC kinetics measurement, respectively; the green trace is the result of applying a 25-point smoothing filter to the black trace computed as the difference of the averaged absorption spectra, further enhancing the S/N and revealing the assigned transitions. * designates potential ^{13}C isotopologue.

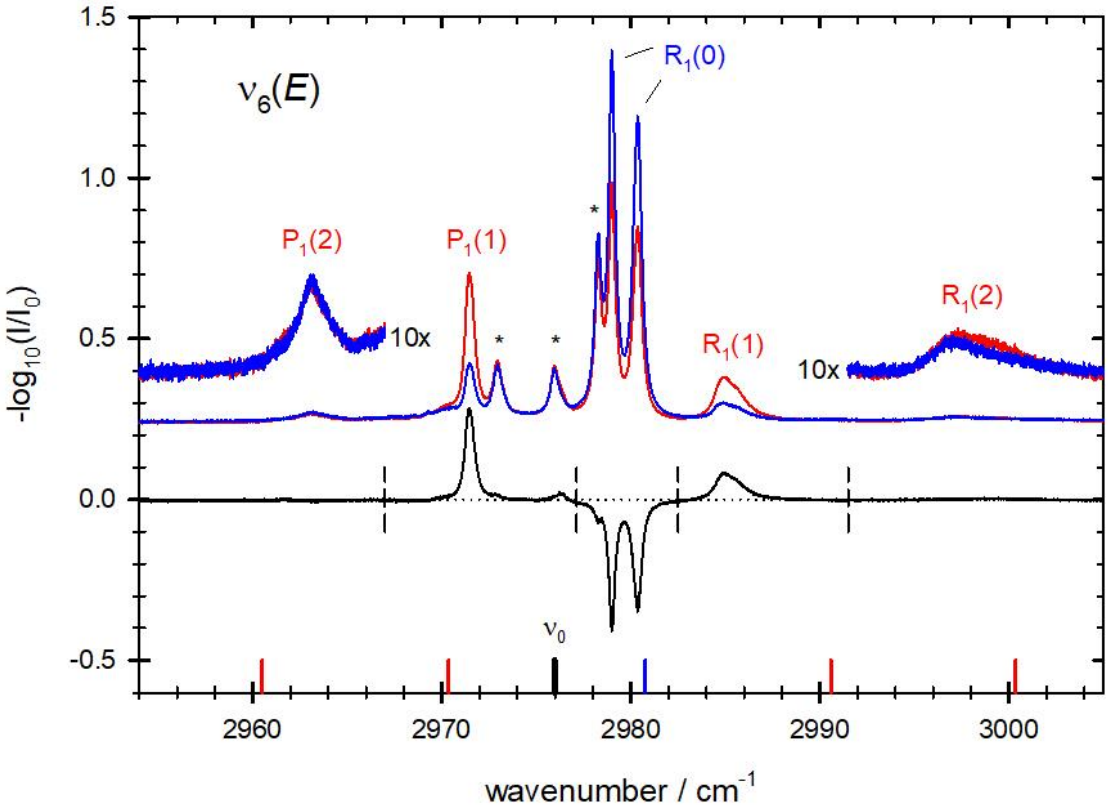

Figure S4. High-resolution (0.02 cm^{-1}) FTIR spectra of the ν_6 (asymmetric methyl C–H stretch) mode of propyne isolated in solid pH_2 and assigned rovibrational transitions. The red, blue, and black traces correspond to absorption spectra of the as-deposited sample (t=0) and equilibrated sample after ~6.5 h ($t\rightarrow\infty$), and the difference spectrum (A_0–A_∞), respectively, recorded using a relatively concentrated sample [Expt. 5; 289(16) ppm, d=2.51(3) mm, T=1.72(2) K] as compared to Fig. 3. These spectra are the initial and final data shown in Fig. 5(b). Peak assignments and gas-phase line positions are shown in blue and red for *ortho*- and *para*-propyne transitions, respectively; the gas-phase spectrum is shifted by the predicted vibrational matrix shift of -4.90 cm^{-1}. Transitions marked by asterisks (*) are tentatively assigned to non-rotating propyne molecules. Integration regions are chosen based on the peak phases in the difference spectrum and are depicted by vertical dashed lines.

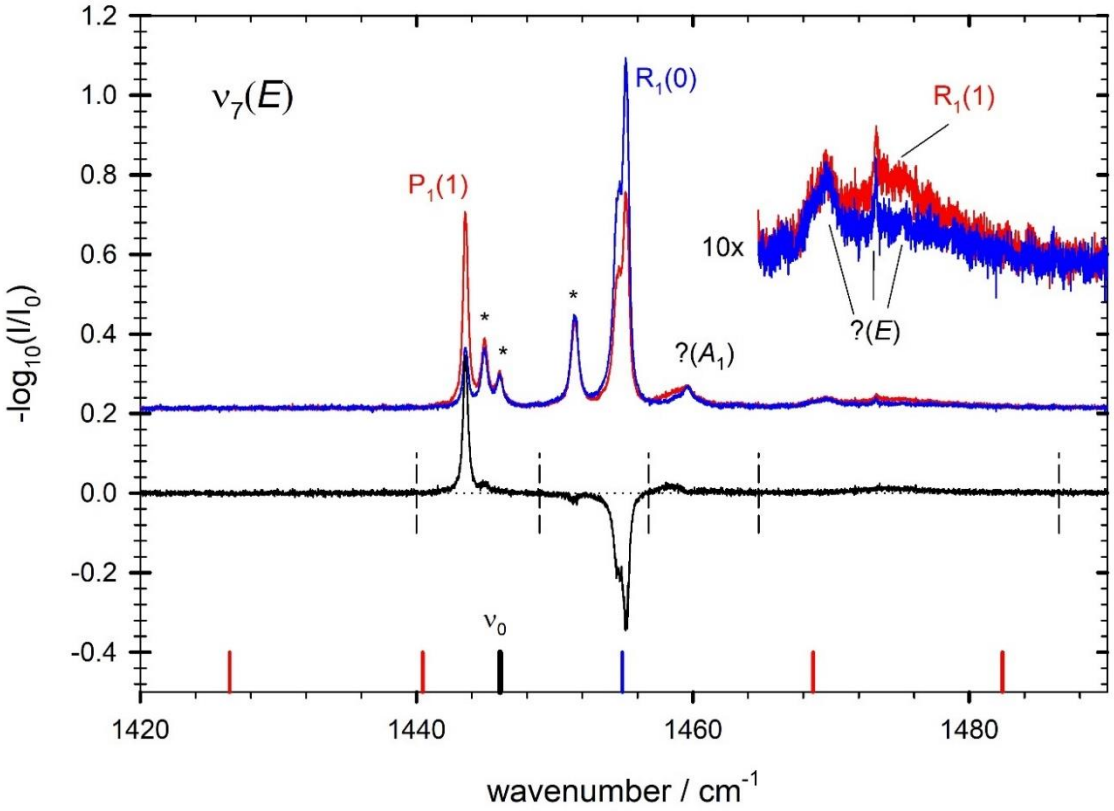

Figure S5. High-resolution (0.03 cm^{-1}) FTIR spectra of the ν_7 (methyl CH_3 rocking) mode of propyne isolated in solid *p*H_2 showing rovibrational assignments. The red, blue, and black traces correspond to absorption spectra of the as-deposited sample (t=0) and equilibrated sample after ~8.3 h ($t\rightarrow\infty$), and the difference spectrum (A_0–A_∞), respectively, recorded using a single concentrated sample [Expt. 6; 200(39) ppm, d=2.5(2) mm, T=1.70(1) K]. These spectra are the initial and final data shown in Fig. 5(c). Peak assignments and gas-phase line positions are shown in blue and red for *ortho*- and *para*-propyne transitions, respectively; the gas-phase spectrum is shifted by the predicted vibrational matrix shift of -4.24 cm^{-1}. Transitions marked by asterisks (*) are tentatively assigned to non-rotating propyne molecules. Integration regions are chosen based on the peak phases in the difference spectrum and are depicted by vertical dashed lines. Question marks indicate non-rotating and/or possibly overlapping transitions which skew the integrated intensities for kinetics measurements (see Fig. 5(c)), bringing up possible issues in making rovibrational assignments.

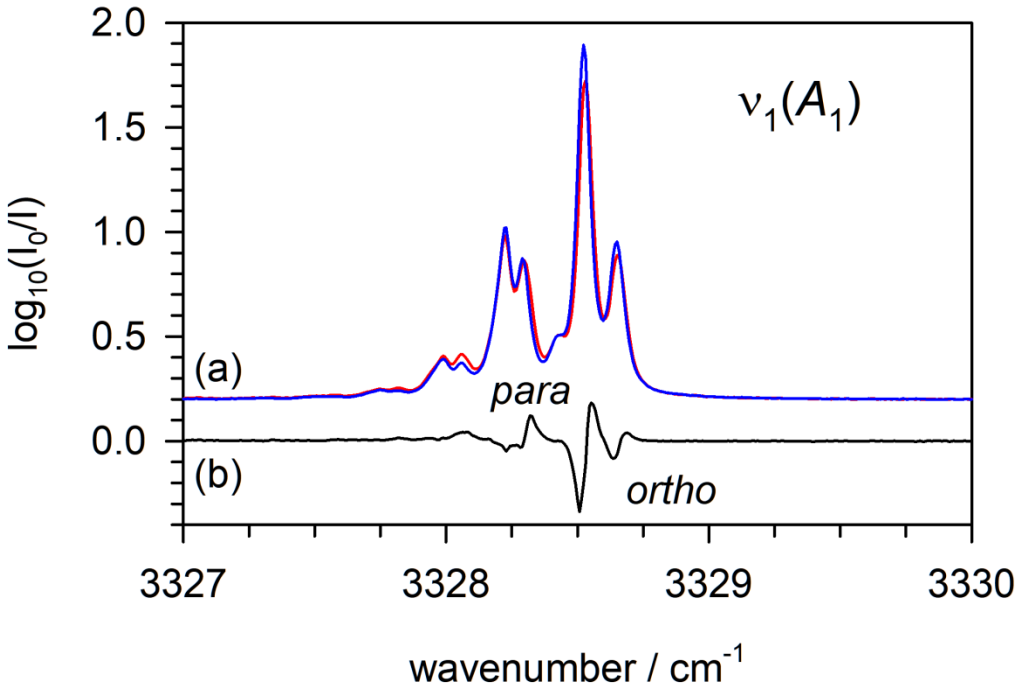

Figure S6. High-resolution (0.02 cm^{-1}) FTIR spectra of the ν_1 (acetylenic C-H stretch) mode of propyne isolated in solid *p*H_2 showing the complicated structure for this A_1 vibrational mode. The red, blue, and black traces correspond to absorption spectra of the as-deposited sample recorded 1.43 and 436 min after deposition, and the corresponding difference spectrum (A_0–A_∞), respectively, recorded using a single sample [Expt. 3; 22(6) ppm, d=1.42(2) mm, T=1.81(2) K]. Note that while the ν_1 vibrational assignment is secure, the additional fine structure and complicated difference spectrum for this A_1-type vibration prevent a clear K-rotational assignment.

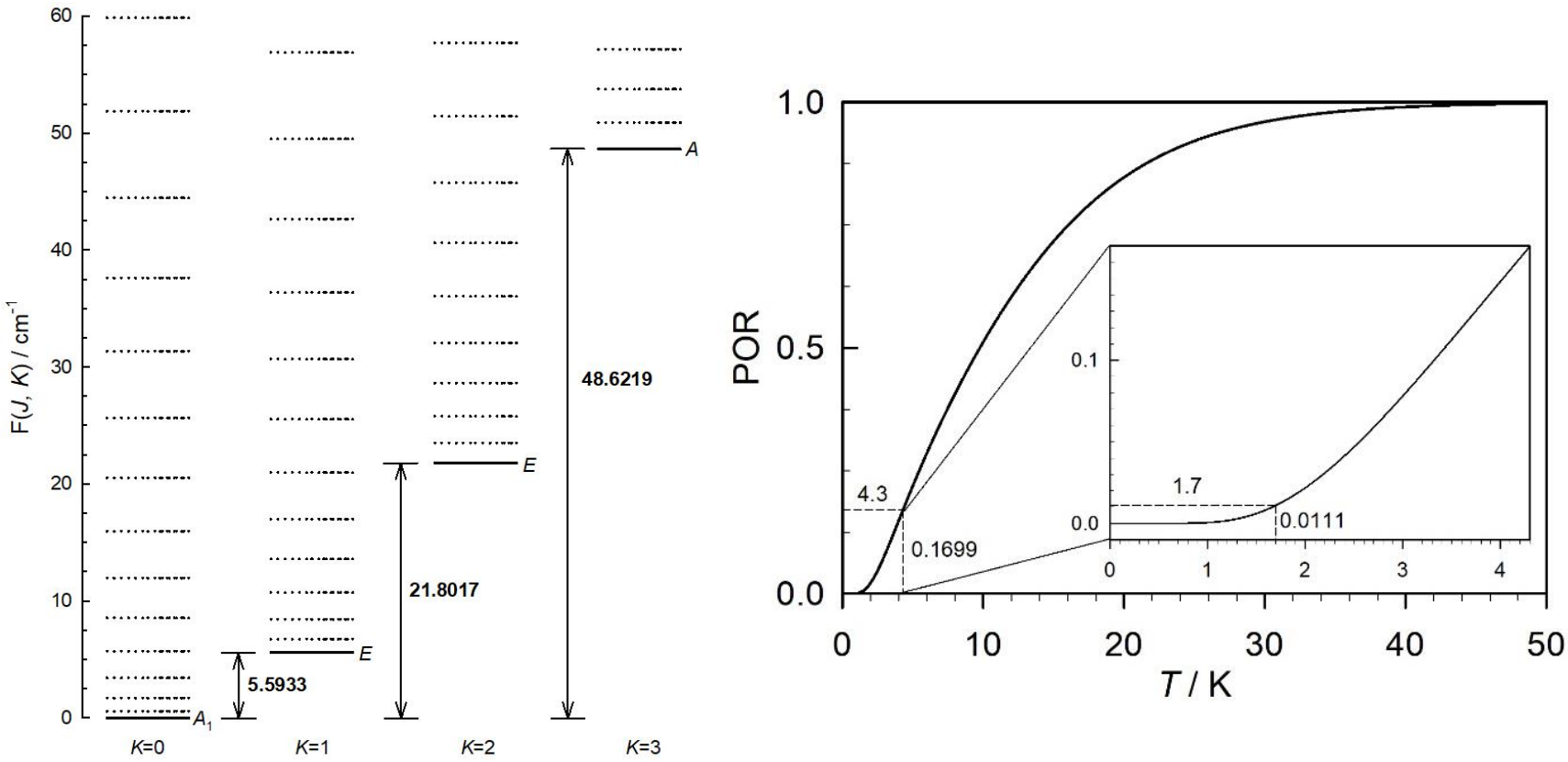

Figure S7. Left: Ground state rotational term values of gas-phase propyne in the free-rotor limit for $J \geq K$=0–3, calculated using the conventional ground state rovibrational constants of Ref. 15 including centrifugal distortion. Solid lines depict the lowest $J=K$ levels, while dotted lines depict higher J-levels in each K-stack. Right: Theoretical *para-to-ortho* ratio (POR) curve for gas-phase propyne as a function of temperature calculated using the rotational term values for J=0–12 and K=0–6 in the ground vibrational state, some of which are shown in the left panel. The inset depicts the POR at liquid He temperatures (0.1699 at 4.3 K), where the predicted POR of propyne is 0.0111 at 1.7 K. Note the high temperature limit approaches unity near ~50 K and decays exponentially to zero at 0 K.

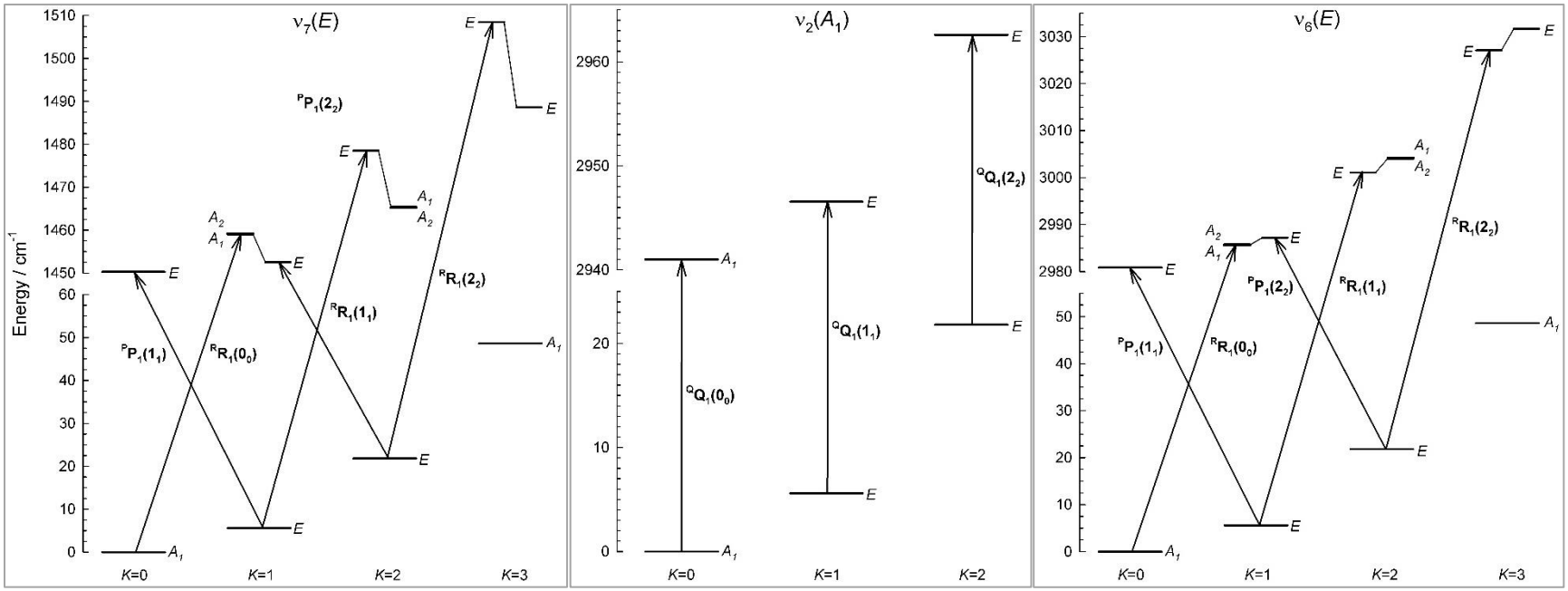

Figure S8. Rovibrational energy diagrams for the ν_7 (Ref. 19), ν_2 (Refs. 16 and 17), and ν_6 (Ref. 18) fundamentals of gas-phase propyne in the free-rotor limit, calculated using the ground state energies shown in Fig. S6. Only the transitions coming out of the lowest J=K=0–2 levels, relevant to the hindered end-over-end rotation of propyne in a low temperature pH$_2$ matrix, are shown. The transitions are labeled using conventional gas-phase notation, which is inaccurate for the description of the single-axis rotation of propyne suspended in solid pH$_2$, as explained in the text. If the K=0–2 levels are populated at 1.7 K, for the parallel (A_1–A_1) band, ν_2, three overlapping peaks corresponding to three closely spaced Q-branch transitions are expected, for which the $Q_1(1)$ and $Q_1(2)$ transitions of *para*-propyne are likely unable to be distinguished from each other, as opposed to the $Q_1(0)$ transition of *ortho*-propyne which is equivalent to the vibrational origin and forbidden in the gas-phase, yet allowed in the pH$_2$ matrix. On the other hand, for perpendicular (A_1–E) bands, such as ν_6 and ν_7, five well-separated peaks are to be expected, namely two P-branch and three R-branch transitions in which the $R_1(0)$ line is the only *ortho*-propyne transition observed; note the effects of first-order Coriolis coupling on the K>0 lines due to the differing sign and magnitude of the Coriolis constants for the ν_6 and ν_7 bands, and that l-type doubling is insignificant, such that the A_1 and A_2 levels are practically degenerate. Adapted from Ref. 11.

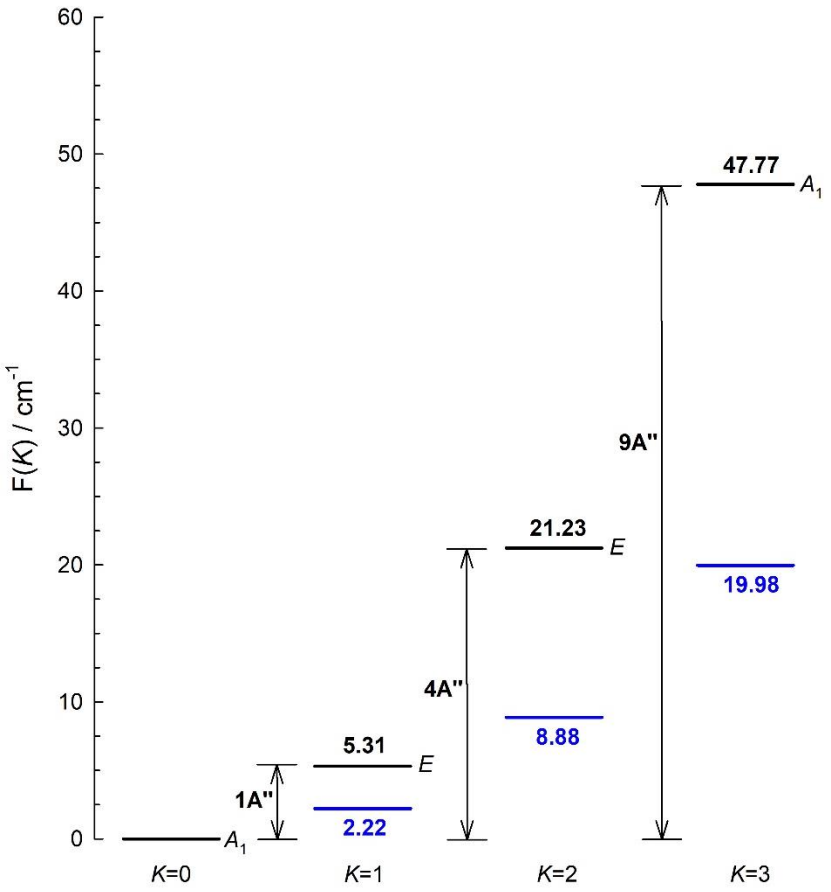

Figure S9. Ground state rotational term values of propyne ($H_3{}^{12}C{}^{12}C_2H$) in the hindered limit for K=0–3 rotor states. Black and blue energy levels correspond to the terms A_0K^2 calculated using the ground vibrational state rotational constant for the gas-phase A_0 = 5.31 cm^{-1} (Ref. 15) and pH$_2$ A_0 = 2.22 cm^{-1} (this work), respectively. Note that 1A'' is equivalent to the energy gap between the lowest *para*(E) and *ortho*(A_1) levels.

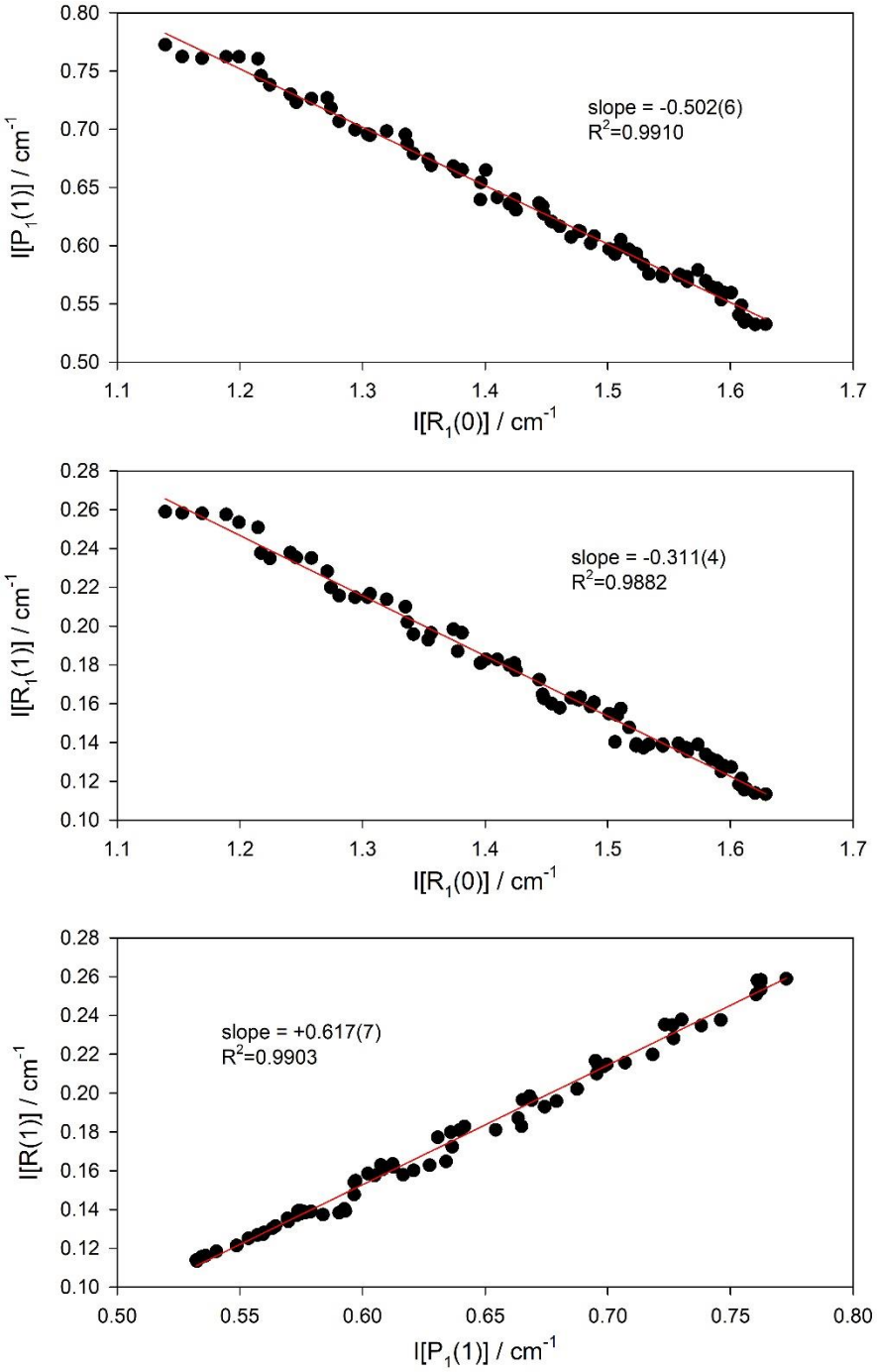

Figure S10. Representative ν_6 intensity-intensity correlation plots (Expt. 5). The top two graphs are generated by plotting the integrated intensities of the $P_1(1)$ and $R_1(1)$ *para*-propyne lines as a function of the $R_1(0)$ *ortho*-propyne line, while the bottom graph is redundant. Negative correlations indicate transitions out of different states, while a positive correlation indicates transitions out of a common lower state. See Table S5.

5. Supporting Tables

Table S1. Experimental parameters: instrument resolution, H_2(g) flow rate, pH$_2$ thickness, per cent hcp content, average propyne concentration, IR bands used to determine concentrations, sample temperatures, and duration of equilibration. Values in parentheses are best estimates of relevant uncertainties in the last significant digit(s). See Section 2. Methods for more details.

Expt.	Filename	Primary Optical Setup	RES / cm^{-1}	Φ_{H_2} / mmol hr^{-1}	d / mm	%hcp	[H_3CC_2H] / ppm	Band(s)	T / K	δt / h
Laramie, WY										
1[a]	AIS02092	GB, KBr, InSb	0.025	280(20)	2.37(7)	52(4)	50(7)	ν_2, ν_6, ν_2+ν_6	1.70(2)	2.35
2	AIS02101	GB, KBr, InSb	0.02	240(30)	2.17(2)	56(5)	74(10)	ν_2, ν_6, ν_2+ν_6	1.72(1)	5.26
3[b]	AIS02114	GB, KBr, InSb	0.02	440(50)	1.42(2)	79(4)	22(6)	ν_1, ν_2, ν_3, ν_6, ν_2+ν_6	1.81(2)	9.74
4	AIS02124	GB, KBr, InSb	0.02	500(100)	3.0(1)	69(3)	33(6)	ν_2, ν_3, ν_6, ν_2+ν_6	1.68(2)	7.89
5	AIS03077	W, CaF_2, InSb	0.02	380(30)	2.51(3)	60(1)	289(16)	ν_6	1.72(2)	6.55
6[c]	AIS03083	GB, KBr, MCT, LPF	0.03	380(30)	2.5(2)	63(5)	200(39)	ν_5, ν_6, ν_7, ν_8, 2ν_9	1.70(1)	8.41
Orsay, France										
7[d]	May2016	GB, KBr, MCT	0.5/0.125	---	0.20(3)	---	423(89)	ν_1, ν_2, ν_3, ν_5, ν_6, ν_8, 2ν_9, ν_2+ν_6	2.8(1)	18
8[d,e]	Dec2019	GB, KBr, MCT	0.5/0.125	---	0.07(1)	---	500(140)	ν_1, ν_2, ν_3, ν_5, ν_6, ν_7, ν_8, 2ν_9, ν_2+ν_6	2.8(1)	25

[a]Observation windows shorter than the effective time constant ($\delta t < \tau_{eff}$) hinder NSC kinetics measurements in this experiment; [b]Etaloning due to relatively thin sample perturbs integrated intensities and, thus, NSC kinetics measurements in this experiment; [c]Placement of a 3861 cm^{-1} long-pass filter (LPF) in the IR beam path and changing the IR light source (intensity) had no significant effect on NSC kinetics; [d]Annealed samples – the approximate time after annealing at ~4 K is given as the equilibration duration; [e]Trace amounts of solid/adsorbed propyne detected ($\nu_1 \approx 3262$ cm^{-1}; Ref. 25) – does not overlap with monomer absorptions.

Table S2. Gas-phase integrated IR band intensities of propyne ($^{12}CH_3{}^{12}C_2H$) from the literature and integration limits employed for determining the concentrations presented in Table S1. Reported uncertainties in the last digit(s) are provided in parentheses. See Table 1 (main text) for vibrational assignments.

Mode	Description	ε_i^{gas} / km mol^{-1}	Limits / cm^{-1}	Ref.
$\nu_1(A_1)$	Acetylenic C–H stretch	45.32(183)	3324.0 – 3320.0	[26]
$\nu_2(A_1)$	Symmetric methylic C–H stretch	17.8(22)[a]	2931.5 – 2937.5	[27,28]
$\nu_3(A_1)$	C≡C stretch	5.31(15)	2137.1 – 2139.2	[26]
$\nu_4(A_1)$[b]	CH_3 deformation	1.42(85)	1382.5 – 1386.1	[27]
$\nu_5(A_1)$	C–C stretch	0.65(17)	929.3 – 930.3	[27]
$\nu_6(E)$	Asymmetric methylic C–H stretch	16.1(19)[a]	2954.0 – 3005.0	[27,28]
$\nu_7(E)$	CH_3 skeletal deformation	17.90(29)	1440.0 – 1486.5	[26]
$\nu_8(E)$	CH_3 skeletal rock	0.5191(178)	1029.6 – 1035.6	[29]
$\nu_9(E)$[c]	H–C≡C bend	90.14(194)	627.0 – 638.0	[26]
$\nu_{10}(E)$	C–C≡C bend	15.9(5)[a]	out of range	[27,28]
$2\nu_9{}^0(A_1)$		16.81(29)	1244.0 – 1260.0	[26]
ν_2 and ν_6[d]		31.88(158)	See above	[26]
ν_4 and ν_7[b,d]		19.3(10)[a]	See above	[27,28]

[a]Weighted average of integrated intensities in Refs. 27,28; [b]Found to produce outliers relative to other modes; [c]IR intensity cutoff near ~600 cm^{-1} due to BaF_2 substrate; [d]As a result of spectral overlap in the gas phase spectra, these values are reported as the total integrated intensity of both bands – see integration windows for the corresponding individual transitions.

Table S3. Pseudo-Voigt lineshape parameters obtained from unweighted least-squares fits to difference spectra ($A_t - A_\infty$) of methylic parallel bands of propyne isotopologues isolated in solid pH$_2$, the number of spectra used in each analysis, and predicted vibration-rotation interaction constants from the peak wavenumbers contrasted with gas-phase values. Values in parentheses are the $1\sigma/\sqrt{N}$ standard errors from statistical analysis of the ν_2 normal isotopologue data, or 1σ standard errors from the least-squares fit otherwise.

Expt.[a]	$\tilde{\nu}_{0,\lambda}$ / cm^{-1}		γ_λ (FWHM) / cm^{-1}		f_λ		N	α^A_{i,pH_2} / cm^{-1}	$\alpha^A_{i,gas}$ / cm^{-1}
	Q(1), E	Q(0), A_1	E	A_1	E	A_1			
				$^{12}CH_3{}^{12}C_2H$ $2\nu_7{}^0$ (A_1)					
5	2871.4(1)	2870.8(2)	0.9(1)	1.1(2)	1.0(2)	0.0(1)	1[b,c]	-0.32(9)	0.043[d]
				$^{12}CH_3{}^{12}C_2H$ ν_2 (A_1)					
1	2934.488(2)	2934.602(2)	0.148(4)	0.182(6)	0.90(1)	0.85(2)	20	---	---
2	2934.4850(7)	2934.605(1)	0.150(1)	0.184(5)	0.92(1)	0.78(2)	45	---	---
3	2934.4868(4)	2934.6031(4)	0.1490(8)	0.148(2)	0.89(1)	0.72(2)	95	---	---
4	2934.4938(6)	2934.613(1)	0.154(1)	0.167(4)	0.86(1)	0.81(1)	83	---	---
Wav.	2934.4885(3)	2934.6039(3)	0.1502(6)	0.157(2)	0.891(3)	0.788(8)	243	0.1154(5)	0.038[d]
				$^{12}CH_3{}^{12}C_2H$ $2\nu_2$ (A_1)					
5	5769.10(3)	5766.77(2)	1.11(7)	1.20(8)	0.0(1)	0.9(2)	1[b,c]	-1.17(2)	0.038[d]
				$^{12}CH_3{}^{12}C_2H$ $\nu_2 + 2\nu_7{}^0$ (A_1)					
5	5814.72(3)	5815.47(4)	0.99(7)	1.30(8)	1.0(1)	0.96(8)	1[b,c]	---	---
				$^{12}CH_3{}^{12}C_2H$ $2\nu_6{}^0$ (A_1)					
5	5906.14(2)	5906.54(2)	0.89(2)	0.74(2)	1.00(4)	0.69(4)	1[b,c]	0.20(1)	0.017[d]
				$^{13}CH_3{}^{12}C_2H$ ν_2 (A_1)					
5	2930.256(5)	2930.368(6)	0.17(1)	0.19(1)	1.0(1)	1.0(1)	1[b]	0.112(8)	---

[a]Parameters were fixed to the average values for each experiment to reduce the number of fitted parameters needed for kinetics analyses; the weighted average (Wav.) ν_2 data provides the best estimate of the line positions and peak widths for spectroscopic purposes; [b]Values listed for the fitted $A_0 - A_\infty$ spectrum: due to low S/N, the first two absorption spectra were averaged together to produce the t=0 spectrum, while the last four spectra were averaged together to produce the $t\rightarrow\infty$ spectrum in order to improve the reliability of the fits; [c]Due to the inherent weakness of the higher order bands (see Ref. 30) the spectra used in these analyses were degraded to 0.1 cm^{-1} resolution, and then a 25-point smoothing filter was applied to the $A_0 - A_\infty$ spectrum to be fit; [d]See Ref. 14 and references therein.

Table S4. Effective first-order *para-to-ortho* NSC time constants obtained via least-squares fits to propyne ($^{12}CH_3{}^{12}C_2H$) NSC kinetic traces for various modes and time constants obtained via a statistical analysis of all measurements. Values in parentheses are either 1σ standard errors from the least-squares fits for individual E/A_1 components or 1σ weighted standard deviations from the weighted average (Wav.) values of the two components for each mode. These data are then grouped for individual modes (Mode Wav.) and globally (Global Wav.) where values in parentheses are $1\sigma/\sqrt{N}$ standard errors accounting for spread in the data and propagation of the 1σ weighted standard deviations from each individual measurement. See note below.

Expt.	τ_{eff} / min								
	$\nu_2(A_1)$			$\nu_6(E)$			$\nu_7(E)$		
	E	A_1	Wav.	E	A_1	Wav.	E	A_1	Wav.
1	270(30)	220(20)	240(20)	170(30)	310(40)	240(30)	not observed		
2	265(7)	270(10)	268(6)	300(15)	281(4)	283(4)	n.o.		
3	290(2)	292(3)	291(2)	230(40)	320(20)	310(20)	n.o.		
4	283(4)	276(5)	280(3)	320(10)	297(3)	299(3)	n.o.		
5		saturated		280(10)	287(8)	286(7)	n.o.		
6		saturated		320(20)	294(6)	296(6)	272(7)	282(4)	279(3)
Mode Wav.			287(11)			292(11)			279(3)
Global Wav.	287(7)								

Note: The weighted average (see Ref. 31 for details) of an observable x with standard deviation σ is defined as

$$\bar{x}_{Wav} = \frac{\sum_i w_i x_i}{\sum_i w_i}$$

in which the weight of the i^{th} measurement is equal to $w_i = 1/\sigma_i^2$. Note also that the weighted standard deviation is

$$\sigma_{Wav} = \frac{1}{\sqrt{\sum_i w_i}}$$

where the reported uncertainty is obtained via summing in quadrature (propagation of error) as

$$\sigma_{reported} = \sqrt{\sum_i \sigma_i^2 + \sigma_{Wav}^2 + s^2}$$

in which the sample variance, s^2, accounts for the spread (or reproducibility) of the data.

Table S5. Intensity-intensity correlation plot parameters obtained from linear ($y(x) = sx + y_0$) least-squares fits to ν_6 integrated intensities (cm^{-1}) of propyne ($^{12}CH_3{}^{12}C_2H$) in solid p-H_2. Values in parentheses are 1σ standard errors obtained from the least-squares fitting procedure or 1σ weighted standard deviations for the weighted average values, considering the spread of the data. Note the sign of each parameter and that $x_0 = -y_0/s$ is a figure of merit that should be nearly equal for two correlation plots with the same abscissae.

Parameter	Expt. 1	Expt. 2	Expt. 3	Expt. 4	Expt. 5	Expt. 6	Wav.
			$P_1(1)$ vs. $R_1(0)$				
y_0	0.240(3)	0.313(1)	0.043(1)	0.1825(8)	1.354(8)	0.755(7)	---
$-s$	0.54(2)	0.477(4)	0.45(2)	0.486(4)	0.502(6)	0.506(9)	0.49(1)
x_0	0.45(1)	0.656(6)	0.095(6)	0.376(3)	2.70(3)	1.49(3)	---
R^2	0.9845	0.9965	0.7859	0.9945	0.9910	0.9748	---
			$R_1(1)$ vs. $R_1(0)$				
y_0	0.110(2)	0.1452(9)	0.0156(8)	0.0819(4)	0.620(6)	0.345(4)	---
$-s$	0.33(1)	0.309(3)	0.29(2)	0.307(2)	0.311(4)	0.319(5)	0.310(5)
x_0	0.34(1)	0.470(5)	0.054(4)	0.266(2)	1.99(3)	1.08(2)	---
R^2	0.9803	0.9964	0.7452	0.9956	0.9882	0.9812	---
			$R_1(1)$ vs. $P_1(1)$				
$-y_0$	0.037(1)	0.0572(4)	0.0125(2)	0.0334(4)	0.217(5)	0.128(3)	---
s	0.61(1)	0.648(2)	0.664(8)	0.631(5)	0.617(7)	0.624(8)	0.641(8)
x_0	0.060(3)	0.0884(7)	0.0188(3)	0.0529(7)	0.352(9)	0.206(5)	---
R^2	0.9924	0.9994	0.9872	0.9954	0.9903	0.9863	---

Table S6. Least-squares fitted parameters obtained from fits to kinetic traces of propyne POR curves calculated using the I[$R_1(1)$]:I[$R_1(0)$] intensity ratio and the corresponding relative linestrength of the ν_6 mode of propyne ($^{12}CH_3{}^{12}C_2H$) in as-deposited solid pH$_2$ samples grown in Laramie. With this, an effective A_0 rotational constant is predicted in addition to the forward (*para→ortho*) and reverse (*ortho→para*) first-order rate constants using effective rate constants for *para-to-ortho* NSC. Values in parentheses are 1σ standard errors from the least-squares fits for the fitted parameters, 1σ standard deviations from error propagation for the calculated values, or 1σ weighted standard errors for the weighted average values in the last digit(s).

Parameter	Expt. 1	Expt. 2	Expt. 3	Expt. 4	Expt. 5	Expt. 6	Wav.
POR_0	0.72(3)	0.725(8)	0.63(3)	0.701(6)	0.744(8)	0.734(8)	---
POR_∞	0.26(2)[a]	0.150(6)	0.015(19)[a,b]	0.128(5)	0.171(6)	0.133(6)	---
$k_{POR}\times10^3$ / min^{-1}	8.3(8)	5.6(1)	8(1)	5.1(1)	5.7(2)	5.1(1)	5.34(65)
R^2	0.9966	0.9989	0.8624	0.9977	0.9967	0.9946	---
A''_{eff} / cm^{-1}	1.6(2)	2.3(1)	5(7)	2.39(9)	2.12(8)	2.4(1)	2.22(55)
$k_{p\rightarrow o}\times10^3$ / min^{-1}	3.4(5)	3.1(1)	3(4)	3.0(1)	3.0(1)	3.0(2)	3.00(9)
$k_{o\rightarrow p}\times10^3$ / min^{-1}	0.9(1)	0.46(2)	0.5(6)	0.38(1)	0.51(2)	0.40(2)	0.44(11)
$k_{eff}\times10^3$ / min^{-1}	4.2(5)	3.54(5)	3.3(2)	3.34(3)	3.49(8)	3.38(7)	3.42(12)

[a]Outliers (see Table S1); [b]Lower limit constrained to the gas-phase POR = 0.0146 at 1.81 K.

Table S7. Experimental POR values for propyne ($^{12}CH_3{}^{12}C_2H$) doped pH$_2$ solids grown in Orsay, measured PORs determined using the ν_6 I[$R_1(1)$]:I[$R_1(0)$] intensity ratio and the corresponding relative line strength ($|s|$ = 0.310(5)), and calculated effective A_0 rotational constants. The initial and equilibrium POR values were measured in the as-deposited sample and several hours after annealing at 4 K, respectively. Values in square brackets are the S/N(RMS) in the ν_6 band region (2954–3005 cm^{-1}) for the listed PORs. Values in parentheses are the 1σ standard deviations obtained via propagation of error in the last digit(s). See note below.

Parameter	Expt. 7	Expt. 8
Initial POR	0.622[8.7]	0.534[3.7]
Equilibrium POR	0.175[8.2]	0.353[4.5]
A''_{eff} / cm^{-1}	3.39(54)	2.02(50)

Note: In this case, the reported error in A''_{eff} is obtained as

$$\sigma_{A''} = A''_{\text{eff}}\sqrt{\left(\frac{\delta T}{T}\right)^2 + \left(\frac{\delta s}{s}\right)^2 + \left(\frac{1}{S/N}\right)^2}$$

where δx is the reported uncertainty in the quantity x.

6. References

(1) Szczepanski, J.; Ekern, S.; Vala, M. Spectroscopy and Photochemistry of the $C_3 \cdot H_2O$ Complex in Argon Matrices. *J. Phys. Chem.* **1995**, *99*, 8002-8012.

(2) Stancik, A. L.; Brauns, E. B. A Simple Asymmetric Lineshape for Fitting Infrared Absorption Spectra. *Vib. Spectrosc.* **2008**, *47*, 66-69.

(3) Lagos, M.; Asenjo, F. A.; Hauyon, R.; Pasten, D.; Moya, P. S. Line Shapes in Infrared Absorption by Solids and by Atomic or Molecular Species Embedded in Solids. *J. Phys. Chem. A* **2010**, *114*, 7353-7358.

(4) Schreier, F. Notes: An Assessment of Some Closed-Form Expressions for the Voigt Function III: Combinations of the Lorentz and Gauss Functions. *J. Quant. Spectrosc. Radiat. Transf.* **2019**, *226*, 87-91.

(5) Kochanov, V. P. On systematic errors in spectral line parameters retrieved with the Voigt line profile. *J. Quant. Spectrosc. Radiat. Transf.* **2012**, *113*, 1635-1641.

(6) Paulson, L. O.; Anderson, D. T. Infrared Spectroscopy of the Amide I Mode of N-Methylacetamide in Solid Hydrogen at 2-4 K. *J. Phys. Chem. B* **2011**, *115*, 13659-13667.

(7) Herzberg, G.: *Molecular Spectra and Molecular Structure - Infrared and Raman Spectra of Polyatomic Molecules*; Krieger Publishing Company: Malabar, Florida, 1988; Vol. Vol. II.

(8) Hollas, J. M.: *High Resolution Spectroscopy*; 2nd ed.; John Wiley & Sons, Ltd.: New York, New York, 1998.

(9) Hougen, J. T. Classification of rotational energy levels for symmetric top molecules. *J. Chem. Phys.* **1962**, *37*, 1433-1441.

(10) Watson, J. D. G. L-Type Doubling: Herzberg Versus Nielsen. *Can. J. Phys.* **2001**, *79*, 521-532.

(11) Lee, Y.-P.; Wu, Y.-J.; Hougen, J. T. Direct Spectral Evidence of Single-Axis Rotation and *ortho*-Hydrogen-Assisted Nuclear Spin Conversion of CH_3F in Solid Para-Hydrogen. *J. Chem. Phys.* **2008**, *129*, 104502.

(12) Lee, Y.-P.; Wu, Y.-J.; Lees, R. M.; Xu, L.-H.; Hougen, J. T. Internal Rotation and Spin Conversion of CH_3OH in Solid Para-Hydrogen. *Science* **2006**, *311*, 365-368.

(13) Lozada-Garcia, R. R.; Ceponkus, J.; Chevalier, M.; Chin, W.; Mestdagh, J.-M.; Crépin, C. Nuclear Spin Conversion to Probe the Methyl Rotation Effect on Hydrogen-Bond and Vibrational Dynamics. *Angew. Chem. Int. Ed.* **2012**, *51*, 6947-6950.

(14) Doney, K. D.; Zhao, D.; Linnartz, H. High-Resolution Infrared Spectra of the ν_1 Fundamental Bands of Mono-Substituted ^{13}C Propyne Isotopologues. *J. Phys. Chem. A* **2018**, *122*, 582-589.

(15) Urban, S.; Pracna, P.; Graner, G. Ground State Energy Levels of Propyne: Conventional Approach and Padé Approximant. *J. Mol. Spectrosc.* **1995**, *169*, 185-189.

(16) McIlroy, A.; Nesbitt, D. J. High-Resolution, Slit Jet Infrared Spectroscopy of Hydrocarbons: Quantum State Specific Mode Mixing in CH Stretch-Excited Propyne. *J. Chem. Phys.* **1989**, *91*, 104-113.

(17) Xing, X.; Reed, B.; Lau, K.-C.; Baek, S.-J.; Bahng, M.-K.; Ng, C. Y. Assignment of Rovibrational Transitions of Propyne in the Region of 2934-2952 cm^{-1} Measured by Two-Color IR–Vacuum Ultraviolet Laser Photoion-Photoelectron Methods. *J. Chem. Phys.* **2007**, *127*, 044313.

(18) Go, J.; Cronin, T. J.; Perry, D. S. A Free-Jet Infrared Double Resonance Study of the Threshold Region of IVR. The ν_6, $\nu_1+\nu_6$, and $2\nu_1$ Bands of Propyne. *Chem. Phys.* **1993**, *175*, 127-145.

(19) Henfrey, N. F.; Thrush, B. A. A High-Resolution Study of the ν_7 Band of Propyne. *J. Mol. Spectrosc.* **1985**, *113*, 426-450.

(20) Silvera, I. F. The Solid Molecular Hydrogens in the Condensed Phase: Fundamentals and Static Properties. *Rev. Mod. Phys.* **1980**, *52*, 393-452.

(21) Abouaf-Marguin, L.; Vasserot, A. M.; Pardanaud, C.; Michaut, X. Nuclear Spin Conversion of H_2O Trapped in Solid Xenon at 4.2 K: A New Assignment of ν_2 Rovibrational Lines. *Chem. Phys. Lett.* **2009**, *480*, 82-85.

(22) Michaut, X.; Vasserot, A.-M.; Abouaf-Marguin, L. Temperature and Time Effects on the Rovibrational Structure of Fundamentals of H_2O Trapped in Solid Argon: Hindered Rotation and RTC Satellite. *Vib. Spectrosc.* **2004**, *34*, 83-93.

(23) Turgeon, P.-A.; Vermette, J.; Alexandrowicz, G.; Peperstraete, Y.; Philippe, L.; Bertin, M.; Fillion, J.-H.; Michaut, X.; Ayotte, P. Confinement Effects on the Nuclear Spin Isomer Conversion of H_2O. *J. Phys. Chem. A* **2017**, *121*, 1571-1576.

(24) Portnov, A.; Blockstein, L.; Bar, I. Vibrational Structure and Methyl C–H Dynamics in Propyne. *J. Chem. Phys.* **2006**, *124*, 164301.

(25) Smith, D. M.; Brainard, J. R.; Grant, M. E.; Lieder, C. A. Infrared-spectra of adsorbed propyne *J. Catal.* **1974**, *32*, 148-154.

(26) Es-Sebbar, E.; Jolly, A.; Benilan, Y.; Farooq, A. Quantitative Mid-Infrared Spectra of Allene and Propyne From Room to High Temperatures. *J. Mol. Spectrosc.* **2014**, *305*, 10-16.

(27) Bode, J. H. G.; Smit, W. M. A.; Visser, T.; Verkruijsse, H. D. The Absolute Infrared Intensities of Propyne-d_0 and Propyne-d_3. *J. Chem. Phys.* **1980**, *72*, 6560-6570.

(28) Kondo, S.; Koga, Y. Infrared-Absorption Intensities of Methyl Acetylene. *J. Chem. Phys.* **1978**, *69*, 4022-4031.

(29) Benzerhouni, K.; Meyer, C.; Dupre, J.; Walrand, J.; Derie, F.; Blanquet, G. Intensity Measurements in the ν_8-Band of Propyne. *J. Quant. Spectrosc. Radiat. Transf.* **1990**, *44*, 245-249.

(30) El Idrissi, M. I.; Lievin, J.; Herman, M.; Campargue, A.; Graner, G. The Vibrational Energy Pattern in Propyne ($^{12}CH_3{}^{12}C_2H$). *Chem. Phys.* **2001**, *265*, 273-289.

(31) Taylor, J. R.: *Introduction to Error Analysis*; 2nd ed.; University Science Books: Sausalito, California, 1997.